

Taking advantage of multiple scattering for Optical Reflection Tomography

Thomas Wasik, Victor Barolle, Alexandre Aubry and Josselin Garnier

Abstract—Optical Diffraction Tomography (ODT) is a powerful non-invasive imaging technique widely used in biological and medical applications. While significant progress has been made in transmission configuration, reflection ODT remains challenging due to the ill-posed nature of the inverse problem. We present a novel optimization algorithm for 3D refractive index (RI) reconstruction in reflection-mode microscopy. Our method takes advantage of the multiply-scattered waves that are reflected by uncontrolled background structures and that illuminate the foreground RI from behind. It tackles the ill-posed nature of the problem using weighted time loss, positivity constraints and Total Variation regularization. We have validated our method with data generated by detailed 2D and 3D simulations, demonstrating its performance under weak scattering conditions and with simplified forward models used in the optimization routine for computational efficiency. In addition, we highlight the need for multi-wavelength analysis and the use of regularization to ensure the reconstruction of the low spatial frequencies of the foreground RI.

Index Terms—Reflection optical phase tomography, ill-posed inverse problem, multiple scattering, total variation regularization, temporal loss function, stochastic proximal-gradient

I. INTRODUCTION

OPTICAL DIFFRACTION TOMOGRAPHY (ODT) is a non-invasive quantitative imaging technique [1]–[3] that has shown promising applications in biology and medical imaging [4], [5]. This technique aims to reconstruct the 3D refractive index (RI) map of a sample by illuminating it from various angles, recovering the complex scattered field using holography techniques [6], and numerically solving the inverse scattering problem of light. This inverse problem is known as an ill-posed problem in transmission and in reflection mode configuration.

ODT was first applied to weakly scattering systems, which can be described using the first Born and Rytov approximations [1], [7]. Under first Born hypothesis, the measurements present a filtering effect [1]. In a transmission configuration, the optical system acts as a low-pass filter of the spatial frequencies of the object along the optical axis, corresponding to the missing-cone problem, while it acts as a high-pass filter in a reflection configuration [8]. In recent years, ODT

techniques have primarily been developed for transmission configurations, with significant efforts focused on simulating stronger scattering regimes and mitigating the missing-cone problem by developing new forward models and iterative techniques for solving the inverse problem [9]–[13].

The application of ODT methods to reflection microscopy would represent a significant breakthrough in the field of non-invasive imaging. Reflection microscopy, in particular, allows for the imaging of thicker samples and enables in vivo imaging [14]. ODT in reflection presents substantial challenges due to the ill-posed nature of the associated inverse problem. In the single scattering regime, only the high spatial frequencies of the object along the optical axis can be reconstructed [8]. On the other hand, in the strongly scattering regime, the forward model becomes non-linear with respect to the RI map [15] and the associated optimization problem is non-convex, providing no guarantee of convergence when employing gradient descent methods, which are commonly used in the literature [9]–[13]. Several techniques have been developed for reflection ODT; however, they are limited by their conditions of application, either requiring a 1D reconstruction [16] or relying on specific setups that do not allow for in vivo imaging [17].

Here, we propose a novel reconstruction algorithm to solve the 3D inverse problem, applicable to a reflection holography configuration with multi-wavelength sources [18]–[20]. The originality of our method lies in the necessity to account for multiple scattering phenomena in order to accurately reconstruct the RI map. It is intuitively based on the idea that, in the multiple scattering regime, the scattering medium itself becomes a source, making it possible to reconstruct a foreground object using the light reflected from the background. The solution to the inverse problem relies on an iterative optimization method that focuses on the low-frequency information of the object. To guide the optimization, special time gating and regularization [21] on the loss will be applied. Our method shares similarities with techniques already explored in microscopy [17], [22], ultrasound [23], [24] and seismology [25], [26], where multiply-scattered waves enable the illumination of structures from behind and can give access to their low-spatial frequency RI distribution in a reflection configuration. In contrast with the existing reflection-ODT method, our approach reconstructs the medium without relying on a known reflector, making it a promising candidate for in vivo imaging. It differs from other reflection-based approaches, which reconstruct layers progressively, imaging deeper structures step by step [27].

T. Wasik is with Institut Langevin at ESPCI Paris, PSL University, CNRS, 75005 Paris, France and with CMAP at Ecole Polytechnique, Institut Polytechnique de Paris, 91120 Palaiseau, France, email:thomas.wasik@polytechnique.edu

V. Barolle is with OWLO SAS, 75014 Paris, France, email:victor@owlo.io

A. Aubry is with Institut Langevin at ESPCI Paris, PSL University, CNRS, 75005 Paris, France, email:alexandre.aubry@espci.fr

J. Garnier is with CMAP at Ecole Polytechnique, Institut Polytechnique de Paris, 91120 Palaiseau, France, email:josselin.garnier@polytechnique.edu

II. MULTIPLE-SCATTERING AND FILTERING EFFECT

Reconstructing RI maps is an ill-posed problem: for similar measured fields, many different RI distributions can be valid solutions. In transmission, this leads to the missing cone problem, which elongates the reconstructed structures. In reflection, the measured signal corresponds mainly to the high spatial frequencies of the sample: the average RI may no longer be detectable.

In this section, we show that, while this limitation holds under the first-order Born approximation, multiple scattering mitigates this effect (even at second order) and constrains the set of possible solutions of our inverse problem. In particular, we demonstrate that reflections from background structures provide additional information about foreground objects, enabling them to be reconstructed more accurately.

A. Measurement as a filtering process

Biological medium can be described by an inhomogeneous scattering potential $V(x, y, z) = k_0^2(n^2(x, y, z) - n_b^2)$, where k_0 is the wavenumber in vacuum, n_b is the background refractive index and $n(x, y, z)$ is the refractive index that we want to recover.

The total field E resulting from interaction with the refractive index $n(x, y, z)$ satisfies Helmholtz equation:

$$(\nabla^2 + k_0^2 n^2(x, y, z))E(x, y, z) = 0 \quad (1)$$

Let us express the complex wavefield as $E = E_{\text{in}} + E_s$ [1], a sum of incident wave solution of the homogeneous Helmholtz equation E_{in} and a scattered field E_s solving:

$$(\nabla^2 + k_0^2 n_b^2)E_s(x, y, z) = U(x, y, z) \quad (2)$$

with Sommerfeld radiation condition. The equation (2) is the homogeneous Helmholtz equation with an internal source term $U(x, y, z) = V(x, y, z)E(x, y, z)$ [8] and it can be solved with the Green's theorem which links the scattered field with the internal source thanks to the homogeneous three-dimensional Green's function $G(x, y, z) = -e^{jn_b k_0 \sqrt{x^2 + y^2 + z^2}} / (4\pi \sqrt{x^2 + y^2 + z^2})$:

$$E_s(x, y, z) = \iiint_{\mathbb{R}^3} U(x', y', z') \times G(x - x', y - y', z - z') dx' dy' dz' \quad (3)$$

In order to express the filtering process operated by the optical system, it is common to apply the first order Born approximation directly to U ($U = VE_{\text{in}}$) in order to obtain a linear relation between the scattered wavefield E_s and the scattering potential V . The filtering effect of the numerical aperture (NA) then directly applies to V . However, in the multiple scattering regime, we emphasize that this filtering operation shall be applied to U and not directly to V .

As a convention and as illustrated in Fig. 1(a), the optical axis is here the z -axis and the measurement of the scattered wavefield is carried out at negative z . If evanescent waves are neglected, the expression of the scattered field (3) can be simplified (Appendix A):

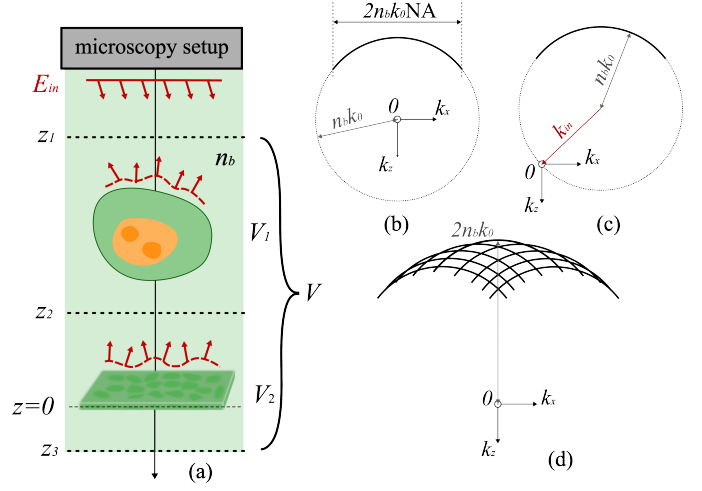


Fig. 1. Schematic representation of the medium to be imaged and illustration of the filtering effects. (a) Illustration of the reflection configuration: the camera is positioned at $z < 0$, while the incident waves propagate along the positive z -direction. The medium is separated into 2 parts: an object to be imaged with potential V_1 and a reflector with potential V_2 . (b) Description of the filtering operation in the (spatial) Fourier domain: only frequencies of $U = VE$ within the semicircle contribute to the measurement. The limited numerical aperture (NA) of the system restricts the acquisition to a portion of the Ewald half-sphere. (c) Filtering effect on V in reflection under the first order Born approximation: the filter is located at high z -frequencies domain in a reflection configuration. (d) Effect of multiple illuminations on V reconstruction under first order Born hypothesis: by multiplying the number of incident waves, filter functions are superposed, providing more information on the object. However, low spatial frequencies remain inaccessible.

$$\mathcal{F}_{2D}[E_s(\cdot, z)](k_x, k_y) \propto \tilde{U} \left(k_x, k_y, \text{sgn}(z) \sqrt{n_b^2 k_0^2 - k_x^2 - k_y^2} \right) \quad (4)$$

where \mathcal{F}_{2D} corresponds to the 2D Fourier transform and the symbol $\tilde{\cdot}$ stands for the 3D Fourier transform. Equation (4) means that it is only possible to recover information in the Ewald sphere of the source U in Fourier space (Fig. 1(b)). In our case, the camera is placed in negative z : only the lower half sphere can be retrieved.

Experimentally, a camera cannot measure the entire spatial frequency spectrum of $E_s(\cdot, z)$, meaning its high-frequency components remain inaccessible in practice. This results in a filtering effect on $E_s(\cdot, z)$ dictated by the numerical aperture (NA) of the measurement system. In the following, we will consider V_{filt} , the reconstructible (i.e., filtered) potential, defined as follows:

$$\tilde{V}_{\text{filt}}(k_x, k_y, k_z) = W_{\text{NA}}(k_x, k_y, k_z) \tilde{U}(k_x, k_y, k_z) \quad (5)$$

$$W_{\text{NA}}(k_x, k_y, k_z) = H_{\text{step}}(-k_z - n_b k_0 \text{NA}) \times \delta(\sqrt{k_x^2 + k_y^2 + k_z^2} - n_b k_0) \quad (6)$$

where H_{step} is the Heaviside step function. W_{NA} is the transfer function of the imaging system. Its support is limited by the NA. It corresponds to the part of the Ewald sphere that can be grasped by the camera. Note that we have here

neglected the potential aberrations induced by the optical system.

B. Information recovered under Born Series approximation

In presence of multiple scattering, the source term $U = EV$ in (2) is too complex to be expressed directly. In order to demonstrate how a multiple scattering system can broaden the spatial filtering effect in comparison with the first-order Born hypothesis, we will use make the second-order Born hypothesis. For this proof-of-concept, we will consider a specific type of medium containing a foreground object V_1 that we will intend to image and a background object V_2 that we will exploit to reach this goal. We thus assume a medium of scattering potential $V = V_1 + V_2$ as described in Fig. 1(a).

1) *First-order Born transfer function:* Under Born's first-order assumption, there is no cross-interactions between the two objects due to the linearity of the model:

$$\begin{aligned} U(x, y, z) &= (V_1(x, y, z) + V_2(x, y, z))E_{\text{in}}(x, y, z) \\ &= V_1(x, y, z)E_{\text{in}}(x, y, z) + V_2(x, y, z)E_{\text{in}}(x, y, z) \\ &= U_1(x, y, z) + U_2(x, y, z) \end{aligned} \quad (7)$$

Let us consider incident plane waves [18]–[20]: $E_{\text{in}}(x, y, z) = e^{j(k_{\text{in},x}x + k_{\text{in},y}y + k_{\text{in},z}z)}$. We can then apply the convolution theorem to get [1]:

$$\tilde{U}_1(k_x, k_y, k_z) = \tilde{V}_1(k_x - k_{\text{in},x}, k_y - k_{\text{in},y}, k_z - k_{\text{in},z}) \quad (8)$$

Because of the reflection configuration $k_{\text{in},z} > 0$ and only a part of the high z -frequencies of V can be recovered by the measurements as illustrated in Fig. 1(c). This filtering phenomenon can nevertheless be mitigated by illuminating the sample with other plane waves at different angles. However, as illustrated in Fig. 1(d), this multi-illumination scheme still does not allow our system to recover the low spatial frequencies of the potential.

Under the first Born approximation, only the potential's high z -frequencies can be recovered by the optical system. The problem is ill-posed in such a way that it is impossible to retrieve the average value of V_1 , for instance. It therefore becomes mandatory to consider a multiple scattering model in order to recover the missing information.

2) *Second-order Born transfer function:* In order to exploit multiply-scattered waves and analytically evaluate their impact on the transfer function, we assume in this subsection that $V_2(x, y, z) = \delta(z)v_2(x, y)$ and that the spatial support of V_1 is localized within a layer $[z_1, z_2]$, with $z_1 < z_2 < 0$. We choose V_2 as planar because we will consider it to be a reflector in our optimization problem, although in practice it never really is and it does not need to be a planar reflector. We only need to be able to represent its reflectivity as the one of a plane reflector.

We model wave propagation by the second-order Born approximation which allows a double interaction of light with the medium:

$$\begin{aligned} U(x, y, z) &= U_1(x, y, z) + U_2(x, y, z) + U_{11}(x, y, z) \\ &\quad + U_{22}(x, y, z) + U_{12}(x, y, z) + U_{21}(x, y, z) \end{aligned} \quad (9)$$

where U_{ij} is defined as:

$$\begin{aligned} U_{ij}(x, y, z) &= V_i(x, y, z) \iiint_{\mathbb{R}^3} G(x - x', y - y', z - z') \\ &\quad \times V_j(x', y', z') E_{\text{in}}(x', y', z') dx' dy' dz'. \end{aligned} \quad (10)$$

We note that, in addition to internal double scattering terms U_{11} and U_{22} , there are cross-interaction terms U_{12} and U_{21} which correspond to scattering paths involving a scattering event with respect to V_1 and a scattering event with respect to V_2 .

In the following, we will demonstrate that these terms encode the low z -frequencies of V_1 . As the V_2 -reflector is in the background relative to the V_1 -medium, the V_2 -reflector will act as a secondary source of waves propagating along the negative z -direction, which are “transmitted” waves from the observer's point of view. In the following, we will refer to this as indirect transmission, and our goal is to exploit this effect to reconstruct V_1 .

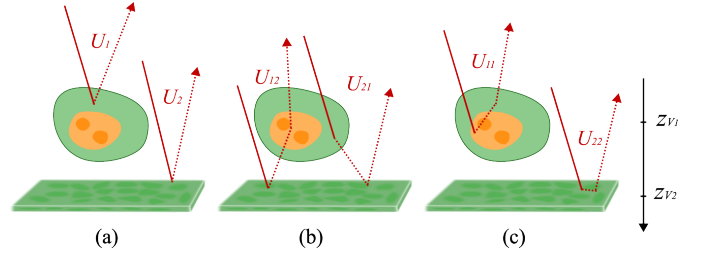


Fig. 2. Decomposition of U according to the different possible light scattering paths under second Born approximation. (a) Representation of single scattering contributions. (b) Crossed terms U_{12} and U_{21} corresponding to successive interactions with the reflector and the target object. (c) Uncrossed double scattering contributions.

The calculation of these cross terms is detailed in Appendix B. Assuming that the supports of V_1 and V_2 are far enough from each other to neglect evanescent waves, we obtain:

$$\tilde{U}_{12}(k_x, k_y, k_z) = \iint_{\mathbb{R}^2} \frac{j\tilde{v}_2(k'_x - k_{\text{in},x}, k'_y - k_{\text{in},y})}{2\sqrt{n_b^2 k_0^2 - k_x'^2 - k_y'^2}} \quad (11)$$

$$\begin{aligned} &\times \tilde{V}_1(k_x - k'_x, k_y - k'_y, k_z + \sqrt{n_b^2 k_0^2 - k_x'^2 - k_y'^2}) dk'_x dk'_y \\ \tilde{U}_{21}(k_x, k_y, k_z) &= \iint_{\mathbb{R}^2} \frac{j\tilde{v}_2(k_x - k'_x, k_y - k'_y)}{2\sqrt{n_b^2 k_0^2 - k_x'^2 - k_y'^2}} \quad (12) \\ &\times \tilde{V}_1(k'_x - k_{\text{in},x}, k'_y - k_{\text{in},y}, \sqrt{n_b^2 k_0^2 - k_x'^2 - k_y'^2} - k_{\text{in},z}) dk'_x dk'_y \end{aligned}$$

where \tilde{v}_2 is the 2D Fourier transform of v_2 . The two terms \tilde{U}_{12} and \tilde{U}_{21} are weighted convolutions between the reflector \tilde{v}_2 and the scattering potential \tilde{V}_1 . These convolution products describe the fact that the presence of v_2 drastically enhances the spectral diversity of the field illuminating V_1 . The amount of information about V_1 encoded in the components U_{21} and U_{12} is therefore increased compared to the first-order Born term U_1 (8). In particular, the spectral diversity provided by v_2 allows the emergence of the low z -frequency components of V_1 in the measured wavefield (5).

This last statement can be illustrated by considering specific reflector configurations that allow the derivation of closed-

form expressions for equations (11) and (12). For instance, if the reflector is uniform (*i.e.* $v_2(x, y) = v_{2o}$), we obtain:

$$\begin{aligned}\tilde{U}_{12}(k_x, k_y, k_z) &= \frac{jv_{2o}}{2\sqrt{n_b^2 k_0^2 - k_{in,x}^2 - k_{in,y}^2}} \\ &\times \tilde{V}_1(k_x - k_{in,x}, k_y - k_{in,y}, k_z + k_{in,z}) \\ \tilde{U}_{21}(k_x, k_y, k_z) &= \frac{jv_{2o}}{2\sqrt{n_b^2 k_0^2 - k_x^2 - k_y^2}} \\ &\times \tilde{V}_1(k_x - k_{in,x}, k_y - k_{in,y}, -\sqrt{n_b^2 k_0^2 - k_x^2 - k_y^2} + k_{in,z})\end{aligned}\quad (13)$$

This equation can also be found directly using the method of images [28]. Applying equation (6), it can be noted that encoded information U_{21} is symmetrical with respect to the $k_z = 0$ axis of the encoded information U_{12} , the filter of this configuration is presented in Fig. 3a.

We can also consider the case of a sinusoidal reflector: $v_2(x, y) = v_{2o}\cos(\gamma x)$ with Fourier transform $\tilde{v}_2(k_x, k_y) = \frac{v_{2o}}{2}(\delta(k_x - \gamma) + \delta(k_x + \gamma))$ with a normal incident wave $E_{in}(k_x, k_y, k_z) = e^{jn_b k_0 z}$. For simplicity, the following expression is evaluated for $\tilde{v}_2(k_x, k_y) = v_{2o}\delta(k_x - \gamma)$ (Fig. 3c):

$$\begin{aligned}\tilde{U}_{12}(k_x, k_y, k_z) &= \frac{jv_{2o}\tilde{V}_1(k_x - \gamma, k_y, -k_z + \sqrt{n_b^2 k_0^2 - \gamma^2})}{2\sqrt{n_b^2 k_0^2 - \gamma^2}} \\ \tilde{U}_{21}(k_x, k_y, k_z) &= \frac{jv_{2o}}{2\sqrt{n_b^2 k_0^2 - (k_x - \gamma)^2 - k_y^2}} \\ &\times \tilde{V}_1(k_x - \gamma, k_y, \sqrt{n_b^2 k_0^2 - (k_x - \gamma)^2 - k_y^2} - n_b k_0)\end{aligned}\quad (14)$$

In the following section, we use these two peculiar configurations to illustrate how the background reflector V_2 can be leveraged to retrieve the low z -frequencies of the foreground structure V_1 .

C. Filtering effect for particular configurations

To that aim, we describe the inverse problem of light scattering as the following optimization problem:

$$\begin{aligned}\hat{\mathbf{V}} &= \arg \min_{\mathbf{V} \in \mathbb{R}^N} \mathcal{L}(\mathbf{V}) \\ \mathcal{L}(\mathbf{V}) &= \|\mathbf{y}_{\text{model}}(\mathbf{V}, \mathbf{E}_{in}) - \mathbf{E}_m\|^2\end{aligned}\quad (15)$$

Here, \mathbf{V} and \mathbf{E}_{in} represent discrete approximation of the corresponding potential V and the incident field E_{in} described respectively as vectors in \mathbb{R}^N and \mathbb{C}^N (the cubic domain is discretized as a uniform grid of size $N = N_x \times N_y \times N_z$). The objective is to minimize a loss function over one illumination to obtain an estimate of the potential V consistent with equations (13) and (14). Equation (15) represents the fidelity term for a single measurement, quantifying the similarity between the field predicted by the forward model, $\mathbf{y}_{\text{model}}$, and the measured scattered field \mathbf{E}_m .

As a forward model, we will use the second order Born as in previous section in order to take into account the predominant multiple scattering paths. The computed total field becomes:

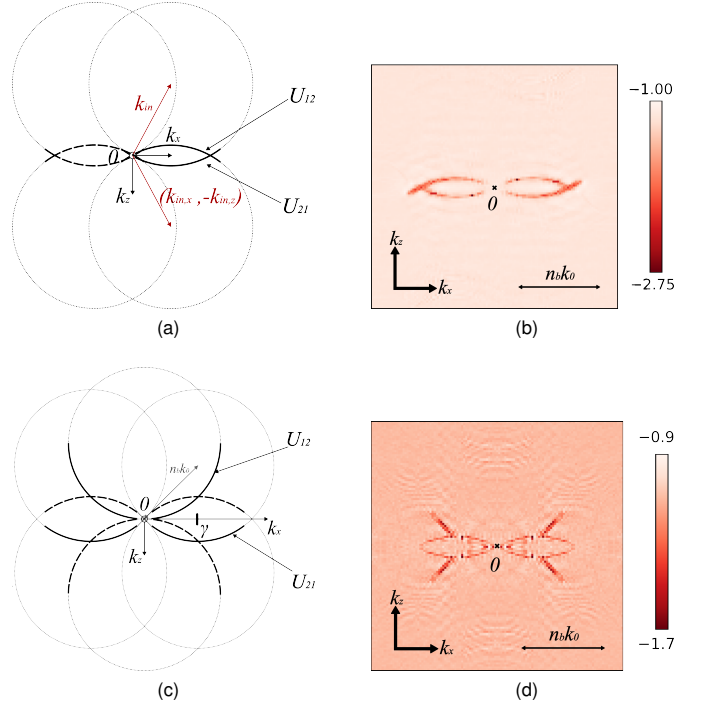


Fig. 3. Support of the spatial frequency spectrum of the object V_1 extracted thanks to the background reflector V_2 . (a) Sketch of these spectral components for a uniform reflector (13) and an incident plane wave of wave vector $\mathbf{k}_{in} = (k_{in,x}, k_{in,y}, k_{in,z})$. (b) Reconstruction error in the spatial Fourier domain between the ground truth V_1 and its estimator \hat{V}_1 deduced from the optimization process in 2D (15) (with red indicating better results). (c) Sketch of the accessible spectral components of V_1 for a cosine-like reflector of frequency γ (14) and a normal incident plane wave ($k_{in,x} = 0$). (d) Same as in panel (b) but for the cosine-like reflector considered in panel (c). In panels (a) and (c), the dashed lines are deduced from the real-value character of V_1 which implies a symmetric spectrum in the Fourier domain. Panels (b) and (d) are numerically obtained in 2D by considering a Dirac potential V_1 whose Fourier spectrum is uniform.

$$\begin{aligned}\mathbf{E}_{\text{Born-2}}(\mathbf{V}, \mathbf{E}_{in}) &= \mathbf{E}_{in} + \mathbf{G}\text{diag}(\mathbf{V})\mathbf{E}_{in} \\ &\quad + \mathbf{G}\text{diag}(\mathbf{V})\mathbf{G}\text{diag}(\mathbf{V})\mathbf{E}_{in} \\ \mathbf{y}_{\text{Born-2}}(\mathbf{V}, \mathbf{E}_{in}) &= \mathbf{H}\text{diag}(\mathbf{V})\mathbf{E}_{\text{Born-2}}(\mathbf{V}, \mathbf{E}_{in})\end{aligned}\quad (16)$$

where $\mathbf{H} \in \mathbb{C}^{N_c \times N}$ is the transfer function describing wave propagation from the sample to the N_c pixels of the camera and $\text{diag}(\mathbf{V}) \in \mathbb{C}^{N \times N}$ the square diagonal matrix whose diagonal elements are given by the components of \mathbf{V} .

In real space, this model involves convolution (or matrix) products, which are computationally expensive. However, this can be bypassed by moving to Fourier space and using Fourier transform of Green function: $\mathbf{G} = \mathbf{F}^\dagger \text{diag}(\tilde{\mathbf{G}}) \mathbf{F} \in \mathbb{C}^{N \times N}$. Here, $\mathbf{F} \in \mathbb{C}^{N \times N}$ is the Fourier transform operator, which is efficiently computed in practice using the Fast Fourier Transform (FFT) algorithm. The computational cost of the forward model is then reduced as it only involves a succession of term-by-term products and FFT operations.

Because of the singularity of the Green's function in Fourier space, we use modified versions $\tilde{\mathbf{G}}^L \in \mathbb{C}^N$, as defined in Refs. [12], [29], [30] to ensure computation stability. This modified Green's function correspond to cropped version in

real space, and a twofold zero-padding is required to ensure accurate computation.

In the following, we will attempt to solve (15) using the gradient descent algorithm. However, the forward model (16) is a second-order polynomial function of V , and gradient descent does not have theoretical guarantees to converge to a global solution of (15). To circumvent this problem and to illustrate the information that can be recovered from the system without dealing with convergence issues (which will be addressed in the next sections), we will fix the background reflector in the simulation as the ground truth.

The model used to calculate the ground truth field is the Lippmann-Schwinger forward model described in Ref. [29]. For sake of illustration of the filtering effect operated by our imaging method, the scattering potential V_1 that we consider here is a Dirac point, as it gives rise to a uniform spectrum in Fourier space. Figures 3(b) and (d) show the reconstruction error between the estimated potential \hat{V}_1 and its ground truth V_1 in Fourier space for the uniform and sinusoidal reflectors V_2 . A quantitative agreement is found between \hat{V}_1 and V_1 over the spatial frequencies captured by the imaging system. The recovered spatial frequency spectra of V nicely match with our analytical predictions (13) and (14) sketched in Figs. 3(a) and (c), respectively. In particular, it illustrates how the presence of reflector V_2 enables multiply scattered trajectories that can be leveraged for retrieving the low z -frequency components of the foreground object V_1 .

III. RECONSTRUCTION ALGORITHM

As discussed in the previous section, an internal background reflector helps to retrieve the low-frequency information from the object in the foreground. However, this information can only be obtained by analyzing the multiply scattered components of the reflected wavefield because the single scattering contribution does not contain the low spatial frequencies of the foreground object. As a result, for reflection-mode ODT, the forward model cannot be linear, making the optimization problem non-convex. Gradient descent algorithms, such as stochastic gradient descent (SGD) or even FISTA [31], therefore lack theoretical guarantees for convergence.

In this section, we propose a reconstruction algorithm that enables good reconstruction in reflection configurations despite the non-convexity of the problem. Our approach is based on (i) the introduction of a new loss function that focuses on the low-frequency components of the object to be reconstructed, (ii) the use of Total Variation (TV) regularization (a commonly applied method [21], [32] that constrains the reconstruction to block-wise behavior) in the foreground region only (i.e. between z_1 and z_2 in Fig. 1), and (iii) a proximal algorithm based on the Adam optimizer [33] ensuring a better convergence despite the non-convexity of the problem.

A. A temporal loss function to focus on low-frequency information

As illustrated in equation (9), the total information recovered is a sum of terms which encode different pieces of information: U_1 encodes high z -frequencies of the object V_1 (8) while U_{12} (11) and U_{21} (12) encode its low z -frequencies. In the ideal case, if V_2 is known, then we can reconstruct both low and high frequencies of the object. However, in practice, the orders of magnitudes of these two terms can be very different, leading to difficulties for the reconstruction of the low z -frequencies of the foreground object if V_2 is too small. We could assume that V_2 is on average much larger than V_1 , but this is not necessarily the case in reality. Ideally, the terms related to direct reflection with the object should be separated from those containing cross interactions between the reflector and the object to be imaged. This can be done by considering the reflected wavefield in the time domain, as it can be done in ultrasound with broadband signals [23].

In optical microscopy, the time-dependence of the reflected wavefield can be retrieved by low coherence interferometry [34].

An alternative strategy is to perform a polychromatic measurement of the wavefield using a spectrometer [35], [36] or a swept source laser [37], [38] as in spectral domain OCT.

In this way, E_m can be measured at different temporal frequencies ω . In post-processing, an inverse Fourier transform with respect to ω can then provide the time-dependent wavefield $E_m(t)$ that would be obtained if the sample was illuminated by a coherent incident wave-packet.

With V_1 in the foreground and V_2 in the background, the ballistic term U_1 and crossed terms U_{12} and U_{21} can be associated with different central times-of-flight $t_1 \sim 2n_b z_{V_1}/c$ and $t_2 \sim 2n_b z_{V_2}/c$, with z_{V_1} and z_{V_2} , the central depths of the foreground object V_1 and the background reflector V_2 (Fig. 2). This assumption is valid in a weakly scattering regime in which the echo time t is directly proportional to the depth z of the associated reflector. Otherwise, high-order multiple scattering would lead to a large temporal dispersion of the incident wave packet [39]–[41], making their discrimination impossible on a time-of-flight time basis.

By considering the i^{th} Born order forward model, we have:

$$\begin{aligned} \mathbf{E}_m(t) &= \mathcal{F}_\omega^{-1}[\mathbf{E}_m(\omega)](t) \\ \mathbf{y}_{\text{Born-}i}(\mathbf{V}, \mathbf{E}_{\text{in}}, t) &= \mathcal{F}_\omega^{-1}[\mathbf{y}_{\text{Born-}i}(\mathbf{V}, \mathbf{E}_{\text{in}}, \omega)](t) \end{aligned}$$

We then define a new temporal loss function over multiple incident illuminations [20]:

$$\mathcal{L}(\mathbf{V}, t) = \sum_{j=1}^{N_{\text{in}}} \mathcal{L}_j(\mathbf{V}, t) \quad (17)$$

$$\mathcal{L}_j(\mathbf{V}, t) = \|\mathbf{y}_{\text{Born-}i}(\mathbf{V}, \mathbf{E}_{\text{in},j}, t) - \mathbf{E}_{m,j}(t)\|^2, \quad (18)$$

and the fidelity term of the loss function becomes

$$\mathcal{L}_{\text{fid}}(\mathbf{V}, \gamma) = \mathcal{L}(\mathbf{V}, t_2) + \gamma \mathcal{L}(\mathbf{V}, t_1) \quad (19)$$

The purpose of this loss function is not to treat the information from direct reflection (associated with time t_1) and the reflection from the background reflector (associated with time

t_2) with equal importance. In fact, if the reflector has a low reflectivity, the model will prioritize the reconstruction of the high spatial frequencies of the object, which may cause the optimization process to become inefficient. t_1 and t_2 can be considered as point or as time intervals. In practice, the use of time interval leads to better reconstruction results.

By considering the problem from a temporal perspective, we can weight the two effects. When γ is small, the impact of the direct reflection from the object is reduced. As a result, the information about the object to be imaged becomes a nonlinear function of its spatial low frequencies, effectively "forcing" the model to focus on a solutions depending on the object's low-frequency components. It becomes even possible, by adjusting γ , to recover both high and low frequencies of the object, improving the reconstruction quality of the sample. Nevertheless, it is important to note that minimizing (19) remains a non-convex problem, which can be challenging even for classical gradient descent algorithms. We address this issue in the next section.

B. Regularization and optimization algorithm

The non-convexity of the loss function leads to the possibility of multiple local minima or saddle points of the loss landscape in (19). The use of a regularization method is equivalent to the use of *a priori* information in order to reduce the number of the possible solutions and facilitate the convergence process of gradient descent based methods. The objective function to minimize in our problem becomes:

$$\mathcal{L}_{\text{ODT}}(\mathbf{V}, \gamma, \tau) = \mathcal{L}(\mathbf{V}, t_2) + \gamma \mathcal{L}(\mathbf{V}, t_1) + \tau \mathcal{R}(\mathbf{V}) \quad (20)$$

in which \mathcal{R} denotes the regularization term and τ is the regularization parameter.

A commonly used regularization term is the Total Variation loss (TV) [32] which is today commonly used for ODT in transmission configuration [10], [21]. This regularization encourages the reconstruction of piecewise constant potentials. The idea is to discourage the reconstruction of noisy objects and improve the sparsity of the reconstruction. Noise can arise, for example, if the reflector is not smooth, making the reconstruction task more difficult. The TV regularization term is:

$$\mathcal{R}_{\text{TV}}(\mathbf{V}) = \sum_{i,j,k} \left\{ ([\mathbf{V}]_{i+1,j,k} - [\mathbf{V}]_{i,j,k})^2 + ([\mathbf{V}]_{i,j+1,k} - [\mathbf{V}]_{i,j,k})^2 + ([\mathbf{V}]_{i,j,k+1} - [\mathbf{V}]_{i,j,k})^2 \right\}^{1/2}$$

Total variation regularization is not a differentiable function over the entire space, which prevents the straightforward use of standard gradient descent methods. One possible approach is to use the subgradient to define a descent method, but this can lead to instabilities during the optimization process and decrease the convergence speed [33].

A widely used optimization approach for ODT in transmission configuration is proximal algorithms [42], which allows the iterative optimization of a loss function composed of a differentiable and a non-differentiable term. Let $\mathbf{V}^{(k)}$ be

the estimator of \mathbf{V} at iteration k . The idea is to split each optimization step into two parts:

- (i) A standard gradient descent step is first performed:

$$\mathbf{V}^{(k)} \leftarrow \mathbf{V}^{(k)} - \alpha \nabla \mathcal{L}_{\text{fid}}(\mathbf{V}^{(k)}, \gamma)$$

- (ii) The proximal operator is then applied:

$$\mathbf{V}^{(k+1)} \leftarrow \text{prox}_{\alpha\tau\mathcal{R}}(\mathbf{V}^{(k)}),$$

which corresponds to the minimization of:

$$\text{prox}_{\alpha\tau\mathcal{R}}(\mathbf{V}^{(k)}) = \arg \min_{\mathbf{V} \in \mathbb{R}^N} \left\{ \frac{1}{2} \|\mathbf{V}^{(k)} - \mathbf{V}\|^2 + \alpha\tau\mathcal{R}(\mathbf{V}) \right\}$$

The proximal operator for TV regularization has the advantage of being well-documented [21], [43].

FISTA and variants are gradient descent or stochastic gradient descent based algorithms. This class of algorithms are designed for convergence of convex loss functions. Reflection ODT being a non convex problem, it was natural to search for a proximal algorithm based on an optimizer efficient for non-convex optimization.

In that respect, an adequate tool is the Adam optimizer [44] which is an adaptive learning rate method. This optimizer is suitable for stochastic gradient descent which allows a reduction of the memory requirement for the optimization process. Moreover, Adam showed better efficiency in non-convex optimization compared to Nestervov stochastic gradient descent algorithm [45], [46].

The challenge with adaptive algorithms lies in the fact that the learning rate depends on the parameter being optimized, thereby requiring a proximal operator that accounts for this dependency. Ref. [33] introduces a method called *ProxGen* that extends proximal gradient algorithms to adaptive optimization techniques such as Adam. Based on this approach, we will use the following proximal algorithm in our methodology:

Algorithm 1 Reflection ODT algorithm: *ProxGen*

input : $\mathbf{V}^{(0)}$, α , ϵ , β_1 , β_2 , γ and τ

Initialize $\mathbf{m}_0 = 0$ and $\mathbf{v}_0 = 0$

for $k = 1, 2, \dots, N_{\text{epoch}}$ **do:**

 Choose randomly an index $i_k \in \{0, \dots, N_{\text{in}}\}$

$\mathbf{g}_k \leftarrow \nabla \mathcal{L}_{\text{fid}, i_k}(\mathbf{V}^{(k-1)}, \gamma)$

$\mathbf{m}_k \leftarrow \beta_1 \mathbf{m}_{k-1} + (1 - \beta_1) \mathbf{g}_k$

$\mathbf{v}_k \leftarrow \beta_2 \mathbf{v}_{k-1} + (1 - \beta_2) (\mathbf{g}_k \circ \mathbf{g}_k)$

$\mathbf{V}^{(k)} \leftarrow \arg \min_{\mathbf{V} \in \mathbb{R}^N} \left\{ \langle \mathbf{V}, \mathbf{m}_k \rangle + \tau \mathcal{R}(\mathbf{V}) + \frac{\|\mathbf{V} - \mathbf{V}^{(k-1)}\|_{\mathbf{v}_k + \epsilon}^2}{2\alpha} \right\}$

return The prediction $\mathbf{V}^{(N)}$

In the algorithm we have introduced a new norm as follows: $\|\mathbf{x}\|_{\mathbf{a}}^2 = \langle \mathbf{x}, \mathbf{a} \circ \mathbf{x} \rangle$ where \circ denotes the element-wise (Hadamard) product. The hyperparameters of the algorithm are: the learning rate ϵ , the momentum parameters β_1 and β_2 , the weight factor γ , and the regularization parameter τ . The last line of the algorithm corresponds to a minimization

problem, which can be reformulated using a new proximal operator:

$$\begin{aligned} \mathbf{V}^{(k)} &\in \arg \min_{\mathbf{V} \in \mathbb{R}^N} \left\{ \langle \mathbf{V}, \mathbf{m}_k \rangle + \tau \mathcal{R}(\mathbf{V}) + \frac{\|\mathbf{V} - \mathbf{V}^{(k-1)}\|_{\mathbf{v}_k + \epsilon}^2}{2\alpha} \right\} \\ &= \text{prox}_{\frac{\tau}{\alpha} \mathcal{R}}^{\mathbf{v}_k + \epsilon} \left(\mathbf{V}^{(k-1)} - \frac{\alpha}{\mathbf{v}_k + \epsilon} \mathbf{m}_k \right) \end{aligned} \quad (21)$$

with $\text{prox}_{\mathbf{h}}^{\mathbf{a}}(\mathbf{z}) = \arg \min_{\mathbf{x}} \{h(\mathbf{x}) + \frac{1}{2}\|\mathbf{x} - \mathbf{z}\|_{\mathbf{a}}^2\}$ and the division is performed element-wise. This minimization problem is convex and can be solved by the proximal algorithm [47]. The gradient of the objective function is $(\mathbf{v}_k + \epsilon)(\mathbf{x} - \mathbf{z})$ and the Lipschitz constant is $L_k = \max(\mathbf{v}_k + \epsilon)$.

The algorithm to compute efficiently \mathbf{V}_k is then:

Algorithm 2 Proximal calculus

```

input :  $\mathbf{V}^{(k-1)}$ ,  $\alpha$ ,  $\epsilon$ ,  $\mathbf{m}_k$ ,  $\mathbf{v}_k$  and  $\tau$ 
 $\mathbf{V}_{\text{prox}}^{(k,0)} = \mathbf{V}^{(k-1)}$ 
 $\mathbf{z}_k = \mathbf{V}^{(k-1)} - \frac{\alpha}{\mathbf{v}_k + \epsilon} \mathbf{m}_k$ 
for  $t = 1, 2, \dots, T$  do:
     $\mathbf{g}_t \leftarrow (\mathbf{v}_k + \epsilon)(\mathbf{V}_{\text{prox}}^{(k,t-1)} - \mathbf{z}_k)$ 
     $\mathbf{V}_{\text{prox}}^{(k,t)} \leftarrow \text{prox}_{\tau \mathcal{R}}(\mathbf{V}_{\text{prox}}^{(k,t-1)} - \frac{1}{\max(\mathbf{v}_k + \epsilon)} \mathbf{g}_t)$ 
return  $\mathbf{V}^{(k)} = \mathbf{V}_{\text{prox}}^{(k,T)}$ 

```

The parameter T defines the number of iterations for Algorithm 2, thereby controlling its convergence behavior. In practice, we set T to be large and apply a stopping criterion which corresponds to the relative change from one iteration to the next:

$$\frac{\|\mathbf{V}_{\text{prox}}^{(k,t)} - \mathbf{V}_{\text{prox}}^{(k,t-1)}\|}{\|\mathbf{V}_{\text{prox}}^{(k,t)}\|} \leq \delta \quad (22)$$

with $\delta = 10^{-6}$ in all following simulations.

C. Simulation results

To validate our reconstruction algorithm, we applied it to 2D simulations for computational efficiency. 3D-simulated medium result are presented at the end of the section. For both 2D and 3D cases, to ensure consistency with the theoretical framework—which assumes the convergence of the Born series—the refractive index deviations are set to $\Delta n = 0.01$. The surrounding medium has a refractive index $n_b = 1.33$. We consider incident plane waves with angles confined within a numerical aperture of $\text{NA} = 0.8$, and wavelengths ranging from 800 to 875 nm.

For both 2D and 3D, the ground truth is, as above, generated using a Lippmann-Schwinger forward model with a modified Green's function $\tilde{\mathbf{G}}^L$ [12], [30]. The use of these modified Green's functions requires adding a padding region with a refractive index of n_b , whose length matches that of the sample. The gradient for our reconstruction is calculated by using the autograd functionality of torch library [48]. For each reconstruction, the reflector is not known in advance and the starting refractive index map is always a uniform medium with a refractive index equal to n_b .

1) *2D simulation:* To evaluate the effectiveness of our approach, we tested our reconstruction algorithm on 2D simulated samples with a resolution of $dx = dz = 200$ nm in a cube of size $N_x = N_z = 161$. Samples under study mimic the refractive index distribution of a cell. We have taken $N_{\text{in}} = 80$ incident waves taken uniformly and sampled over 11 wavelength to guarantee a sufficient temporal resolution and discriminate the direct object echo and the background reflector components.

The reflector placed in our simulation behind the sample corresponds to an interface with average refractive index $n = 1.335$, to which we add Gaussian noise with standard deviation $\delta n = 0.002$.

For optimal convergence, all 2D hyperparameters have been carefully tuned for Figs. 4-6. We also validated our approach using simulated noisy observations. Further details can be found in Appendix C.

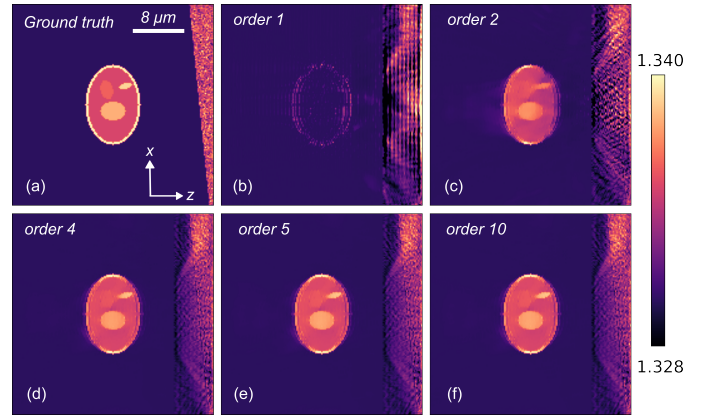


Fig. 4. Reconstruction of sample composed of a cell and a reflector depending of the forward model with the *ProxGen* algorithm and the weighted temporal loss function ($\gamma = 0.1$). A minimum regularizer is used to improve the quality of reconstruction. The reconstruction is impossible by using first order Born approximation.

2) *Choice of the forward model:* Choosing an appropriate forward model for the optimization algorithm is essential for improving the quality of the refractive index reconstruction. Indeed, this model should closely account for the multiple-scattering contribution in order to accurately reconstruct the sample. Fig. 4 illustrates this fact by displaying the result of our optimization algorithm for different forward models. Each model involves a different order of the Born approximation. Not surprisingly, the first-order Born model (Fig. 4(b)) only grasps the high spatial frequencies of the sample and only provides an image of the external surface of the cell. Remarkably, the second-order Born model reveals the intra-cellular components (Fig. 4(c)). Nevertheless, the reconstruction remains imperfect due to discrepancies between the real light propagation and the forward model. Those imperfections can be mitigated by increasing the degree of complexity of the forward model (Fig. 4(d)-(f)). The 5th-order Born series forward model (Fig. 4(d)-(f)) offers a good compromise between the accuracy of the refractive index map and its computational complexity.

3) *Regularization strategies:* In the following, total variation (TV) regularization is applied only in the region of

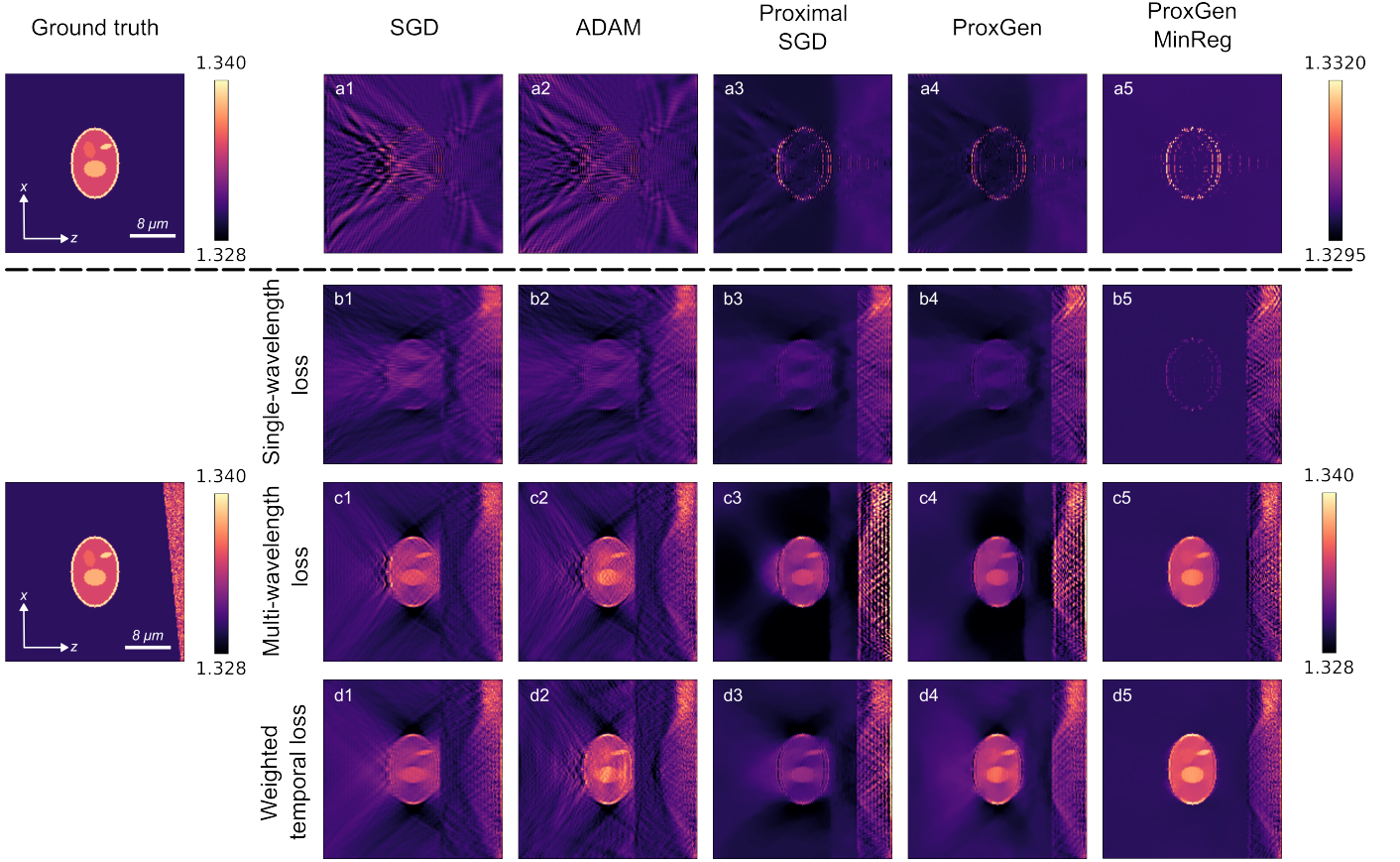


Fig. 5. 2D reconstruction results for different configurations with order 5 Born forward model. Each column corresponds to an optimization algorithm. Row (a) shows the results for the single-wavelength loss without a reflector. Since the results for different loss functions without reflector are similar, they are not displayed here. The last three rows present the reconstructions using different loss functions with ground truth including a reflector. The unweighted temporal loss is not shown, as it produces results similar to the multi-wavelength loss (row (c)); the Fourier transform does not significantly impact the results. The weighted temporal loss shown here corresponds to equation (17) with a coefficient $\gamma = 0.1$.

the object V_1 that we aim to reconstruct. Additionally, a differentiable regularization term, referred to as *Minimum regularization*, is introduced. This term prevents predictions below the refractive index n_b , acting as a Ridge regression for points with a refractive index lower than n_b . Since this regularization is differentiable, it can be easily integrated into the temporal loss function. This additional regularization corresponds to a positivity constraint. Choi *et al.* [2] actually demonstrated that it reduced the underestimation of the refractive index in a transmission configuration. The TV and minimum regularization procedures are applied to the V_1 -object region (contained in the layer $[z_1, z_2]$ in Fig. 1(a)) but not to the V_2 -reflector (layer $[z_2, z_3]$ in Fig. 1(a)). Indeed, we are only interested in retrieving the reflector's reflectivity, not its exact refractive index which is out of reach in the present case.

Figure 5 illustrates the improvement in the object reconstruction achieved by applying aforementioned strategies. The first row (Fig. 5(a)) highlights the challenge of reconstructing the sample without a reflector, even when using various iterative optimization techniques. In this case, the scattering potential remains trapped in a local minimum or flat region, preventing accurate reconstruction. As previously highlighted, the low-spatial frequencies of the object can be hardly re-

trieved in such a configuration.

However, the second row (Fig. 5(b)) shows that simply adding a reflector is not sufficient if the temporal aspect is not considered. In a single-wavelength experimental setup, the singly-scattered term U_1 and U_2 , as well as the second-order crossed terms U_{12} and U_{21} , cannot be disentangled. This mixing prevents the convergence of the optimization algorithms.

The last two rows of Fig. 5 demonstrate that temporal resolution is essential for accurate cell reconstruction. The multi-wavelength loss (Fig. 5(c)) corresponds to a broadband loss function that incorporates multiple wavelengths:

$$\mathcal{L}_B(\mathbf{V}) = \sum_{\omega} \|\mathbf{y}_{\text{Born-}i}(\mathbf{V}, \mathbf{E}_{\text{in}}, \omega) - \mathbf{E}_{\text{m}}(\omega)\|^2.$$

Due to Parseval's theorem, $\mathcal{L}_B(\mathbf{V})$ is actually equivalent to a temporal loss integrated over all times-of-flight:

$$\mathcal{L}_B(\mathbf{V}) = \sum_t \|\mathbf{y}_{\text{Born-}i}(\mathbf{V}, \mathbf{E}_{\text{in}}, t) - \mathbf{E}_{\text{m}}(t)\|^2.$$

All time points are here weighted equally. While this approach enables good cell reconstruction, further improvement can be achieved using a weighted temporal loss, as described in (19) and illustrated by Fig. 5(d). The TV regularization

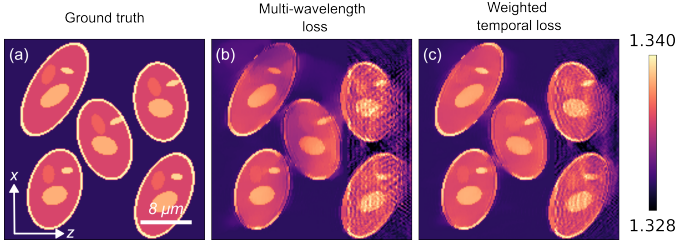


Fig. 6. Reconstruction of complex samples thanks to the *ProxGen* algorithm by using different loss functions. Here the reflector corresponds to the background cells at the right. The regularization (TV by proximal and minimum regularization) are applied at the left of the image and not for the reflector. As in previous cells the initialization corresponds to uniform medium.

is here essential to reconstruct correctly the sample as the reconstruction is noisy without it. While SGD and Adam-based gradient descent methods yield similar results for the multi-wavelength loss, Adam-based methods perform better when using the weighted temporal loss. The results improve further when applying minimal regularization, which prevents the refractive index from falling below n_b .

4) *Importance of a weighted temporal loss:* Unlike alternative methods that reconstruct the refractive index of an object using a deterministic reflector [17], our approach does not require any prior knowledge on it. Indeed, this reflector can belong to the inspected medium. The refractive index distribution can be reconstructed, even when the background reflector is highly irregular and initially unknown.

Additionally, this algorithm can be applied to more complex samples. For instance, we can consider a 2D sample made up of multiple cells, and attempt to reconstruct the upstream cells by using the background cells as reflectors. Examples of such reconstructions are shown in Fig. 6, where we can observe that the weighted temporal loss (Fig. 6(c)) leads to more satisfactory results than the multi-wavelength loss (Fig. 6(b)) in this case [see the comparison with ground truth displayed in Fig. 6(a)]. Since the energy received at both echo times is similar, it becomes more difficult for the model to focus on reconstructing the object's low-frequency components. On the contrary, the weighted temporal loss enhances the strength of back-scattered echoes and leads to a better image the sample.

Thus, despite being far from the ideal case of a planar reflector, our method enables high-quality reconstruction of refractive index maps. Moreover, the use of a weighted loss allows for the reconstruction of both low and high spatial frequencies, effectively mitigating the missing cone problem commonly encountered in transmission. However, as shown in Fig. 5, achieving a good reconstruction requires the presence of a reflector (and therefore a complex medium), as well as a temporal loss (hence a multi-illumination device), unlike in a transmission configuration.

5) *3D reconstruction:* To demonstrate the scalability of our model, we also simulated 3D reconstructions. The sample under study is displayed in Fig. 7(a). The simulation domain is a cube of size $N_x = N_y = N_z = 101$ of resolution $dx = dy = dz = 200$ nm. The simulated illumination sequence involves 80 illuminations spirally distributed within

a pupil of numerical aperture $NA = 0.8$. Each illumination is repeated for 11 wavelengths uniformly distributed between 800 and 875 nm.

The forward model used in our optimization process is still a 5th order Born model since we remain in a weakly scattering regime. The optimization is performed over 1000 epochs to ensure convergence, although a good reconstruction can already be achieved after 400 epochs. The reconstruction was efficiently carried out on an RTX 6000 Ada GPU with 48GB of VRAM. Each epoch took 30 seconds, which is longer than for an equivalent transmission reconstruction, as wave propagation needs to be computed for multiple wavelengths.

Due to the long training time, we fine-tuned our optimization algorithm on a smaller cube and applied the same hyperparameters to the larger one. We used a learning rate of $\epsilon = 2 \times 10^{-5}$, momentum parameters $(\beta_1, \beta_2) = (0.9, 0.999)$, and a weight factor $\gamma = 0.1$ to generate the figure. The result of the optimization process is displayed in Fig. 7.

It appears that in 3D, it is still possible to obtain good reconstructions of cells in the foreground, by using cells in the background. The average values of the various substructures remain consistent with the ground truth. However, the reconstruction quality is not as good as in 2D, due to the larger number of parameters to optimize and the increased difficulty in tuning the hyperparameters.

IV. CONCLUSION

We have introduced a novel optimization algorithm for 3D refractive index reconstruction in reflection-mode microscopy. Our method is based on the exploitation of multiple light scattering. More precisely, our approach consists in leveraging the light backscattered by deep reflectors to map the refractive index distribution in the foreground. The background reflector is *a priori* unknown, and its reflectivity is simultaneously reconstructed as part of the training process. This approach is therefore a promising candidate to reach quantitative in vivo optical imaging.

The ill-posed character of the problem is circumvented by a weighted temporal loss in order to focus on the low frequency part of the object and by using positivity constraint and sparsity regularization to converge to a good minimum. The resulting reconstructions closely match the ground truth across both low and high spatial frequencies, highlighting the effectiveness of the weighted temporal loss.

We implemented a 2D and 3D version to demonstrate its effectiveness in simulations. To remain consistent with the theory, we restricted our study to weakly scattering media and used relatively simple forward models compared to transmission ODT [49]. However, in practice, this method could involve more advanced forward models for larger refractive index contrast as Multi-layer Born [10], modified Born series [50] or Lippmann-Schwinger Model [12]. Whether it can be adapted to a more strongly scattering regime still needs to be demonstrated, either in simulation or experimentally.

We have also demonstrated the necessity of multi-wavelength analysis in reflection to achieve the required temporal approach. As a result, ODT in reflection will be

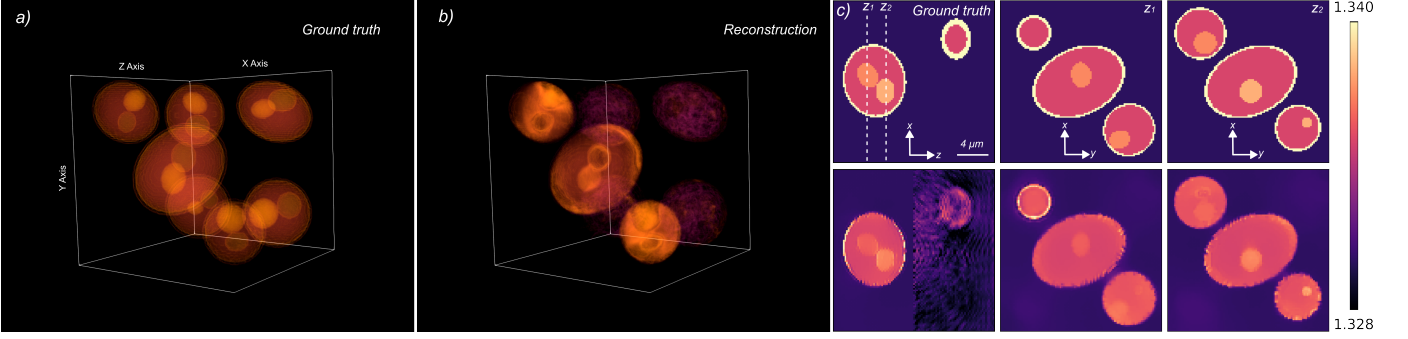


Fig. 7. 3D Reconstruction with the proposed method of $20 \times 20 \times 20 \mu\text{m}$ sample constituted by several simulated cells. Figure (a) shows the ground truth 3D rendering, figure (b) corresponds to the reconstruction and (c) a series of ground truth and prediction cuts. The inhomogeneity of the reconstructed cells in figure (b) is due to the fact that the reconstructed background cells correspond to an equivalent reflectivity of lower optical index than the ground truth. An animation is available in the supplementary materials.

more time-expensive than transmission approaches but will be rewarding since we will have access to both the low and high spatial frequencies of the sample. This also helps overcome the missing cone issue inherent to transmission configurations.

Beyond optical microscopy, the proposed approach can be leveraged to map the local wave speed in any field of wave physics for which a frequency- or time-resolved measurement of the reflection matrix is possible [51], [52]. Indeed, not only is the local wave speed a quantitative marker for ultrasound diagnosis [53] but it is also, for instance, an important monitoring parameter of tectonic motion [54] and volcanic eruption [55] in geophysics. In each of this field, multiple scattering is far from being negligible [56], [57] and its inclusion in the forward model would be extremely rewarding for quantitative imaging. This is the principle of full wave-form inversion [58] but we here show how such brute force strategies would benefit from physically-grounded loss functions and simplifications of the forward model in order to guarantee the convergence of the inversion process.

ACKNOWLEDGMENTS

A.A. is grateful for the funding provided by the European Research Council (ERC) under the European Union's Horizon 2020 research and innovation program (grant agreement no. 819261, REMINISCENCE project).

APPENDIX A

FILTERING OPERATION ON SOURCE TERM

This section is a proof of the filtering effect of measurement in transmission and reflection configuration. The proof is the same as in *Emil Wolf* [1] work, but without the first order Born hypothesis.

We express the scattered field as a function of the source term:

$$E_s(x, y, z) = \iiint_{\mathbb{R}^3} U(x', y', z') \times G(x - x', y - y', z - z') dx' dy' dz' \quad (3)$$

Since the object to be imaged is of finite size, we assume that V is supported in $[z_1, z_3]$ and that we measure the scattered field for $z \in (-\infty, z_1) \cup (z_3, +\infty)$.

Since we are measuring E_s at a fixed z , it is natural to look for calculations based on the 2D Fourier transform of the 3D Green's function. Thus we have [59]:

$$\begin{aligned} \iint_{\mathbb{R}^2} G(x, y, z) e^{-j(k_x x + k_y y)} dx dy &= \frac{j}{2\kappa(k_x, k_y)} e^{j\kappa(k_x, k_y)|z|} \\ G(x, y, z) &= \iint_{\mathbb{R}^2} \frac{j}{2\kappa(k_x, k_y)} e^{j(k_x x + k_y y + \kappa(k_x, k_y)|z|)} dk_x dk_y \end{aligned} \quad (23)$$

with κ defined as:

$$\kappa(k_x, k_y) = \begin{cases} \sqrt{n_b^2 k_0^2 - k_x^2 - k_y^2} & \text{if } n_b^2 k_0^2 \geq k_x^2 + k_y^2, \\ j\sqrt{k_x^2 + k_y^2 - n_b^2 k_0^2} & \text{if } n_b^2 k_0^2 < k_x^2 + k_y^2. \end{cases}$$

κ is the z -wavelength of the Green function with two modes: a propagative mode and an evanescent one.

In the following, we rewrite (23) taking into account the fact that $z \in (-\infty, z_1) \cup (z_3, +\infty)$ and $z' \in \text{supp}(V)$

$$G(x - x', y - y', z - z') = \iint_{\mathbb{R}^2} \frac{j}{2\kappa(k_x, k_y)} \times e^{j(k_x(x-x') + k_y(y-y') + \text{sgn}(z)\kappa(k_x, k_y)(z-z'))} dk_x dk_y \quad (24)$$

By injecting (24) into (3) we obtain:

$$E_s(x, y, z) = \iint_{\mathbb{R}^2} A(k_x, k_y, z) \times e^{j(k_x x + k_y y + \text{sgn}(z)\kappa(k_x, k_y)z)} dk_x dk_y \quad (25)$$

$$A(k_x, k_y, z) = \frac{j}{2\kappa(k_x, k_y)} \iiint_{\mathbb{R}^3} U(x', y', z') \times e^{-j(k_x x' + k_y y' + \text{sgn}(z)\kappa(k_x, k_y)z')} dk_x dk_y dk_z \quad (26)$$

By developing (25), we can express A by the 2D Fourier transform of $E_s(\cdot, z)$

$$\mathcal{F}_{2D}(E_s(\cdot, z))(k_x, k_y) e^{-\text{sgn}(z)j\kappa(k_x, k_y)z} = A(k_x, k_y, z) \quad (27)$$

The equation is difficult to express in simple terms, because κ is a complex number. However, we assume that we are measuring with z far enough away from the support of V that the evanescent waves are negligible (i.e. $A(k_x, k_y, k_z) \approx 0$ if $n_b^2 k_0^2 < k_x^2 + k_y^2$). Consequently, κ is real, and we can express A directly as the Fourier transform of U :

$$A(k_x, k_y, z) = \frac{j\tilde{U}(k_x, k_y, \text{sgn}(z)\sqrt{n_b^2 k_0^2 - k_x^2 - k_y^2})}{2\sqrt{n_b^2 k_0^2 - k_x^2 - k_y^2}} \quad (28)$$

And by combining (28) and (27) we obtain:

$$\mathcal{F}_{2D}(E_s(\cdot, z))(k_x, k_y) \propto \tilde{U}(k_x, k_y, \text{sgn}(z)) \sqrt{n_b^2 k_0^2 - k_x^2 - k_y^2} \quad (4)$$

We finally found that we can only measure the Ewald sphere of the source U as shown in [8] under the Fraunhofer approximation.

APPENDIX B

FILTERING OPERATION UNDER SECOND BORN APPROXIMATION

Let us begin by examining the U_{12} term, which represents an interaction with the reflector V_2 followed by an interaction with the potential V_1 . We can express U_{12} as:

$$\begin{aligned} U_{12}(x, y, z) &= V_1(x, y, z) H_2(x, y, z) \\ H_2(x, y, z) &= \iiint_{\mathbb{R}^3} G(x - x', y - y', z - z') \\ &\quad \times V_2(x', y', z') E_{\text{in}}(x', y', z') dx' dy' dz' \\ &= \iint_{\mathbb{R}^2} G(x - x', y - y', z) \\ &\quad \times v_2(x', y') E_{\text{in}}(x', y', 0) dx' dy' \end{aligned} \quad (29)$$

H_2 corresponds to a new incident wave from the reflector V_2 . By injecting the 2D Fourier transform of the Green function [59] (23), assuming that z is small enough to neglect evanescent waves (since $\text{supp}(V_1) = [z_1, z_2]$ we assume here that z_2 is far enough from 0) and by using convolution theorem, we can express H_2 in a 2D integral form:

$$\begin{aligned} \mathcal{F}_{2D}(H_2(\cdot, z)) &= \frac{j e^{j \sqrt{n_b^2 k_0^2 - k_x^2 - k_y^2} |z|}}{2 \sqrt{n_b^2 k_0^2 - k_x^2 - k_y^2}} \tilde{v}_2(k_x - k_{\text{in},x}, k_y - k_{\text{in},y}) \\ H_2(x, y, z) &= \iint_{\mathbb{R}^2} \frac{j \tilde{v}_2(k_x - k_{\text{in},x}, k_y - k_{\text{in},y})}{2 \sqrt{n_b^2 k_0^2 - k_x^2 - k_y^2}} e^{j(k_x x + k_y y)} \\ &\quad \times e^{j \sqrt{n_b^2 k_0^2 - k_x^2 - k_y^2} |z|} dk_x dk_y \end{aligned} \quad (30)$$

By applying a Fourier transform to (29), substituting (30), and simplifying the absolute value due to the support of $V_1(\cdot, z')$ being restricted to $(-\infty, 0)$, we obtain:

$$\begin{aligned} \tilde{H}_2(k_x, k_y, k_z) &= \iint_{\mathbb{R}^2} \frac{j \tilde{v}_2(k'_x - k_{\text{in},x}, k'_y - k_{\text{in},y})}{2 \sqrt{n_b^2 k_0^2 - k_x'^2 - k_y'^2}} \\ &\quad \times \tilde{V}_1(k_x - k'_x, k_y - k'_y, k_z + \sqrt{n_b^2 k_0^2 - k_x'^2 - k_y'^2}) dk'_x dk'_y \end{aligned} \quad (11)$$

The second term U_{21} corresponds to the interaction with V_1 followed by the interaction with the reflector V_2 .

$$\begin{aligned} U_{21}(x, y, z) &= V_2(x, y, z) H_1(x, y, z) \\ H_1(x, y, z) &= \iiint_{\mathbb{R}^3} G(x - x', y - y', z - z') \\ &\quad \times V_1(x', y', z') E_{\text{in}}(x', y', z') dx' dy' dz' \end{aligned} \quad (31)$$

By applying a Fourier transform to U_{21} we have:

$$\begin{aligned} \tilde{U}_{21}(k_x, k_y, k_z) &= \iiint_{\mathbb{R}^3} V_2(x, y, z) H_1(x, y, z) \\ &\quad \times e^{j(k_x x + k_y y + k_z z)} dx dy dz \\ &= \iint_{\mathbb{R}^2} v_2(x, y) H_1(x, y, 0) e^{j(k_x x + k_y y)} dx dy dz \\ &= \iint_{\mathbb{R}^2} \tilde{v}_2(k_x - k'_x, k_y - k'_y) \\ &\quad \times \mathcal{F}_{2D}(H_2(\cdot, z = 0))(k'_x, k'_y) dk'_x dk'_y \end{aligned}$$

In order to get an analytical expression for the Fourier transform U_{12} , we need to express the 2D Fourier transform of H_1 :

$$\begin{aligned} \mathcal{F}_{2D}(H_1(\cdot, z = 0))(k_x, k_y) &= \iint_{\mathbb{R}^2} H_1(x, y, 0) e^{-j(k_x x + k_y y)} dx dy \\ &= \iiint_{\mathbb{R}^3} \iint_{\mathbb{R}^2} G(x - x', y - y', -z') V_1(x', y', z') \\ &\quad \times e^{j(k_{\text{in},x} x' + k_{\text{in},y} y' + k_{\text{in},z} z') - j(k_x x + k_y y)} dx dy dx' dy' dz' \\ &= \iiint_{\mathbb{R}^3} \iint_{\mathbb{R}^2} G(x'', y'', -z') e^{-j(k_x x'' + k_y y'')} dx'' dy'' \\ &\quad \times V_1(x', y', z') e^{j[(k_{\text{in},x} - k_x)x' + (k_{\text{in},y} - k_y)y' + k_{\text{in},z} z']} dx' dy' dz' \\ &= \int_{\mathbb{R}} dz' \left[\iint_{\mathbb{R}^2} G(x'', y'', -z') e^{-j(k_x x'' + k_y y'')} dx'' dy'' \right] \\ &\quad \times \left[\iint_{\mathbb{R}^2} V_1(x', y', z') e^{j[(k_{\text{in},x} - k_x)x' + (k_{\text{in},y} - k_y)y' + k_{\text{in},z} z']} dx' dy' \right] \end{aligned}$$

The first term between square brackets is the 2D Fourier transform of the Green function and defined in eq (23). The second term between square brackets is:

$$\begin{aligned} \iint_{\mathbb{R}^2} V_1(x', y', z') e^{j[(k_{\text{in},x} - k_x)x' + (k_{\text{in},y} - k_y)y' + k_{\text{in},z} z']} dx' dy' \\ = \mathcal{F}_{2D}(V_1(\cdot, z'))(k_x - k_{\text{in},x}, k_y - k_{\text{in},y}) e^{j k_{\text{in},z} z'} \end{aligned}$$

Since the support of $V_1(\cdot, z')$ is in $(-\infty, 0)$, the integral in z' is concentrated on $(-\infty, 0)$ and:

$$\begin{aligned} \mathcal{F}_{2D}(H_1(\cdot, z = 0))(k_x, k_y) &= \int_{\mathbb{R}} \frac{j \mathcal{F}_{2D}(V_1(\cdot, z'))(k_x - k_{\text{in},x}, k_y - k_{\text{in},y})}{2 \kappa(k_x, k_y)} e^{j(k_{\text{in},z} - \kappa(k_x, k_y))z'} dz' \end{aligned}$$

which gives (by ignoring evanescent waves):

$$\begin{aligned} \mathcal{F}_{2D}(H_1(\cdot, z = 0))(k_x, k_y) &= \frac{j}{2 \sqrt{n_b^2 k_0^2 - k_x^2 - k_y^2}} \\ &\quad \times \tilde{V}_1(k_x - k_{\text{in},x}, k_y - k_{\text{in},y}, \sqrt{n_b^2 k_0^2 - k_x^2 - k_y^2} - k_{\text{in},z}) \end{aligned} \quad (32)$$

Finally, we obtain the following formula for U_{21} :

$$\begin{aligned} \tilde{U}_{21}(k_x, k_y, k_z) &= \iint_{\mathbb{R}^2} \frac{j \tilde{v}_2(k_x - k'_x, k_y - k'_y)}{2 \sqrt{n_b^2 k_0^2 - k_x'^2 - k_y'^2}} \\ &\quad \times \tilde{V}_1(\tilde{k}_x - k_{\text{in},x}, \tilde{k}_y - k_{\text{in},y}, \sqrt{n_b^2 k_0^2 - k_x'^2 - k_y'^2} - k_{\text{in},z}) dk'_x dk'_y \end{aligned} \quad (12)$$

APPENDIX C

NOISE ANALYSIS AND SELECTION OF HYPERPARAMETERS

Since we had to solve an ill-posed inverse problem, longer training times were necessary. To ensure better convergence for method comparison, we fine-tuned the learning rate and trained until 1000 epochs. However, the reconstruction quality becomes acceptable around 400 epochs, even though the loss continues to decrease. The optimal learning rate was generally found to be around $\epsilon = 10^{-5}$. For adaptive methods, the coefficients were set as recommended in Kingma's *et al* work [44] $(\beta_1, \beta_2) = (0.9, 0.999)$. The best coefficient for the total variation loss was fine-tuned for each figure and was around $\tau = 0.1$. This regularization term was applied to the refractive index map normalized between 0 and 1. TV regularization and minimum regularization are not applied on the reflector because it allows better reconstruction of foreground objects.

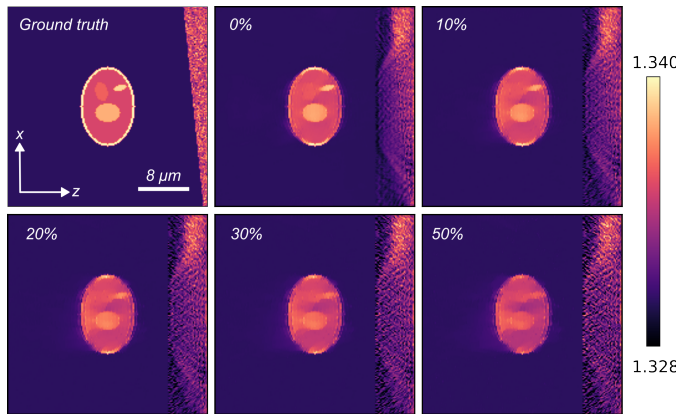


Fig. 8. Evolution of prediction depending on a function of the level of Gaussian noise added to the simulated measure. Despite the loss of precision, the 2D reconstruction of the foreground cell remains consistent with the ground truth. Reconstructions are performed with weighted temporal loss ($\gamma = 0.1$) with *ProxGen* algorithm and minimum regularization.

Despite the use of the weighted temporal loss to focus on the low-frequency signal, the optimization problem is not straightforward and requires more training time than in transmission. Thus our optimization algorithm could be sensitive to noisy measurement. To verify this, we conducted 2D tests by adding noise to the ground truth measurements. As shown in Figure 8, our model remains robust to Gaussian noise up to 50%. The noise level is here defined relatively to the mean of the reflected absolute amplitude.

REFERENCES

- [1] E. Wolf, "Three-dimensional structure determination of semi-transparent objects from holographic data," *Optics communications*, vol. 1, no. 4, pp. 153–156, 1969.
- [2] W. Choi, C. Fang-Yen, K. Badizadegan, S. Oh, N. Lue, R. R. Dasari, and M. S. Feld, "Tomographic phase microscopy," *Nature methods*, vol. 4, no. 9, pp. 717–719, 2007.
- [3] D. Jin, R. Zhou, Z. Yaqoob, and P. T. So, "Tomographic phase microscopy: principles and applications in bioimaging," *JOSA B*, vol. 34, no. 5, pp. B64–B77, 2017.
- [4] P. Y. Liu, L. K. Chin, W. Ser, H. Chen, C.-M. Hsieh, C.-H. Lee, K.-B. Sung, T. Ayi, P. Yap, B. Liedberg *et al.*, "Cell refractive index for cell biology and disease diagnosis: past, present and future," *Lab on a Chip*, vol. 16, no. 4, pp. 634–644, 2016.
- [5] Y. Park, C. Depeursinge, and G. Popescu, "Quantitative phase imaging in biomedicine," *Nature photonics*, vol. 12, no. 10, pp. 578–589, 2018.
- [6] M. K. Kim, "Principles and techniques of digital holographic microscopy," *SPIE reviews*, vol. 1, no. 1, p. 018005, 2010.
- [7] A. Devaney, "Inverse-scattering theory within the rytov approximation," *Optics letters*, vol. 6, no. 8, pp. 374–376, 1981.
- [8] J. M. Coupland and J. Lobera, "Holography, tomography and 3d microscopy as linear filtering operations," *Measurement science and technology*, vol. 19, no. 7, p. 074012, 2008.
- [9] X. Ma, W. Xiao, and F. Pan, "Optical tomographic reconstruction based on multi-slice wave propagation method," *Optics express*, vol. 25, no. 19, pp. 22 595–22 607, 2017.
- [10] M. Chen, D. Ren, H.-Y. Liu, S. Chowdhury, and L. Waller, "Multi-layer born multiple-scattering model for 3d phase microscopy," *Optica*, vol. 7, no. 5, pp. 394–403, 2020.
- [11] M. Lee, H. Hugonnet, and Y. Park, "Inverse problem solver for multiple light scattering using modified born series," *Optica*, vol. 9, no. 2, pp. 177–182, 2022.
- [12] T.-a. Pham, E. Soubies, A. Ayoub, J. Lim, D. Psaltis, and M. Unser, "Three-dimensional optical diffraction tomography with lippmann-schwinger model," *IEEE Transactions on Computational Imaging*, vol. 6, pp. 727–738, 2020.
- [13] U. S. Kamilov, H. Mansour, and B. Wohlberg, "A plug-and-play priors approach for solving nonlinear imaging inverse problems," *IEEE Signal Processing Letters*, vol. 24, no. 12, pp. 1872–1876, 2017.
- [14] R. Weissleder, "A clearer vision for in vivo imaging," *Nature biotechnology*, vol. 19, no. 4, pp. 316–317, 2001.
- [15] M. Born and E. Wolf, *Principles of Optics*, 7th ed. Cambridge University Press, 2003.
- [16] S. Kang, R. Zhou, M. Brelén, H. K. Mak, P. T. So, and Z. Yaqoob, "Reflection-mode optical diffraction tomography for label-free imaging of thick biological specimens," *arXiv preprint arXiv:2202.13668*, 2022.
- [17] T. Li, J. Zhu, Y. Shen, and L. Tian, "Reflection-mode diffraction tomography of multiple-scattering samples on a reflective substrate from intensity images," *Optica*, vol. 12, no. 3, pp. 406–417, Mar 2025. [Online]. Available: <https://opg.optica.org/optica/abstract.cfm?URI=optica-12-3-406>
- [18] Y.-R. Lee, D.-Y. Kim, Y. Jo, M. Kim, and W. Choi, "Exploiting volumetric wave correlation for enhanced depth imaging in scattering medium," *Nat. Commun.*, vol. 14, no. 1, apr 2023. [Online]. Available: <https://www.nature.com/articles/s41467-023-37467-z>
- [19] Y. Zhang, D. Minh, Z. Wang, T. Zhang, T. Chen, and C. W. Hsu, "Deep imaging inside scattering media through virtual spatiotemporal wavefrontshaping," *arXiv:2306.08793*, 2023. [Online]. Available: <https://arxiv.org/abs/2306.08793>
- [20] P. Balondrade, V. Barolle, N. Guigui, E. Auriant, N. Rougier, C. Boccara, M. Fink, and A. Aubry, "Multi-spectral reflection matrix for ultrafast 3d label-free microscopy," *Nature Photonics*, vol. 18, no. 10, pp. 1097–1104, 2024.
- [21] U. S. Kamilov, I. N. Papadopoulos, M. H. Shoreh, A. Goy, C. Vonesch, M. Unser, and D. Psaltis, "Optical tomographic image reconstruction based on beam propagation and sparse regularization," *IEEE Transactions on Computational Imaging*, vol. 2, no. 1, pp. 59–70, 2016.
- [22] S. Kang, Y. Kwon, H. Lee, S. Kim, J. H. Hong, S. Yoon, and W. Choi, "Tracing multiple scattering trajectories for deep optical imaging in scattering media," *Nature communications*, vol. 14, no. 1, p. 6871, 2023.
- [23] T. D. Weber, N. Khetan, R. Yang, and J. Mertz, "Ultrasound differential phase contrast using backscattering and the memory effect," *Applied Physics Letters*, vol. 118, no. 12, Mar. 2021.
- [24] P. Stahli, M. Frenz, and M. Jaeger, "Bayesian approach for a robust speed-of-sound reconstruction using pulse-echo ultrasound," *IEEE Transactions on Medical Imaging*, vol. 40, no. 2, pp. 457–467, Feb. 2021.
- [25] P. Mora, *Inversion=migration+tomography*. Springer Berlin Heidelberg, 1989, pp. 78–101.
- [26] A. E. Malcolm, B. Ursin, and M. V. De Hoop, "Seismic imaging and illumination with internal multiples," *Geophysical Journal International*, vol. 176, no. 3, pp. 847–864, 2009.
- [27] Y. Wang and Y. Rao, "Reflection seismic waveform tomography," *Journal of Geophysical Research: Solid Earth*, vol. 114, no. B3, 2009. [Online]. Available: <https://agupubs.onlinelibrary.wiley.com/doi/abs/10.1029/2008JB005916>
- [28] G. Taraldsen, "The complex image method," *Wave Motion*, vol. 43, no. 1, pp. 91–97, 2005.
- [29] E. Soubies, T.-A. Pham, and M. Unser, "Efficient inversion of multiple-scattering model for optical diffraction tomography," *Optics express*, vol. 25, no. 18, pp. 21 786–21 800, 2017.
- [30] F. Vico, L. Greengard, and M. Ferrando, "Fast convolution with free-space green's functions," *Journal of Computational Physics*, vol. 323, pp. 191–203, 2016.
- [31] A. Beck and M. Teboulle, "A fast iterative shrinkage-thresholding algorithm for linear inverse problems," *SIAM Journal on Imaging*

- Sciences, vol. 2, no. 1, pp. 183–202, 2009. [Online]. Available: <https://doi.org/10.1137/080716542>
- [32] L. I. Rudin, S. Osher, and E. Fatemi, “Nonlinear total variation based noise removal algorithms,” *Physica D: Nonlinear Phenomena*, vol. 60, no. 1, pp. 259–268, 1992. [Online]. Available: <https://www.sciencedirect.com/science/article/pii/016727899290242F>
- [33] J. Yun, A. C. Lozano, and E. Yang, “Adaptive proximal gradient methods for structured neural networks,” in *Advances in Neural Information Processing Systems*, M. Ranzato, A. Beygelzimer, Y. Dauphin, P. Liang, and J. W. Vaughan, Eds., vol. 34. Curran Associates, Inc., 2021, pp. 24365–24378. [Online]. Available: https://proceedings.neurips.cc/paper_files/paper/2021/file/cc3f5463bc4d26bc38eadc8bcffbc654-Paper.pdf
- [34] A. Badon, G. Lerosee, A. C. Boccara, M. Fink, and A. Aubry, “Retrieving time-dependent green’s functions in optics with low-coherence interferometry,” *Physical Review Letters*, vol. 114, no. 2, Jan. 2015.
- [35] M. Choma, M. Sarunic, C. Yang, and J. Izatt, “Sensitivity advantage of swept source and fourier domain optical coherence tomography,” *Opt. Express*, vol. 11, no. 18, pp. 2183–2189, sep 2003.
- [36] S. H. Yun, G. J. Tearney, B. E. Bouma, B. H. Park, and J. F. de Boer, “High-speed spectral-domain optical coherence tomography at 1.3 μm wavelength,” *Opt. Express*, vol. 11, no. 26, pp. 3598–3604, Dec 2003. [Online]. Available: <http://www.opticsexpress.org/abstract.cfm?URI=oe-11-26-3598>
- [37] D. Hillmann, G. Franke, C. Lührs, P. Koch, and G. Hüttmann, “Efficient holoscopy image reconstruction,” *Opt. Express*, vol. 20, no. 19, pp. 21247–21263, Sep. 2012. [Online]. Available: <https://opg.optica.org/oe/abstract.cfm?uri=oe-20-19-21247>
- [38] B. Považay, A. Unterhuber, B. Hermann, H. Sattmann, H. Arthaber, and W. Drexler, “Full-field time-encoded frequency-domain optical coherence tomography,” *Opt. Express*, vol. 14, no. 17, pp. 7661–7669, Aug. 2006. [Online]. Available: <https://opg.optica.org/oe/abstract.cfm?uri=oe-14-17-7661>
- [39] A. Derode, P. Roux, and M. Fink, “Robust acoustic time reversal with high-order multiple scattering,” *Physical Review Letters*, vol. 75, no. 23, pp. 4206–4209, Dec. 1995.
- [40] A. P. Mosk, A. Lagendijk, G. Lerosee, and M. Fink, “Controlling waves in space and time for imaging and focusing in complex media,” *Nat. Photonics*, vol. 6, no. 5, pp. 283–292, may 2012.
- [41] R. K. Wang, “Signal degradation by multiple scattering in optical coherence tomography of dense tissue: a monte carlo study towards optical clearing of biotissues,” *Physics in Medicine & Biology*, vol. 47, no. 13, p. 2281, jun 2002. [Online]. Available: <https://dx.doi.org/10.1088/0031-9155/47/13/307>
- [42] N. Parikh and S. Boyd, “Proximal algorithms,” *Foundations and Trends® in Optimization*, vol. 1, no. 3, pp. 127–239, 2014. [Online]. Available: <http://dx.doi.org/10.1561/24000000003>
- [43] A. Beck and M. Teboulle, “Fast gradient-based algorithms for constrained total variation image denoising and deblurring problems,” *IEEE Transactions on Image Processing*, vol. 18, no. 11, pp. 2419–2434, 2009.
- [44] D. P. Kingma and J. Ba, “Adam: A method for stochastic optimization,” *arXiv preprint arXiv:1412.6980*, 2014.
- [45] S. De, A. Mukherjee, and E. Ullah, “Convergence guarantees for rmsprop and adam in non-convex optimization and an empirical comparison to nesterov acceleration,” 2018.
- [46] M. Zaheer, S. J. Reddi, D. Sachan, S. Kale, and S. Kumar, “Adaptive methods for nonconvex optimization,” in *Advances in Neural Information Processing Systems*. Curran Associates, Inc., 2018, vol. 31. [Online]. Available: <https://papers.nips.cc/paper/2018/hash/8186-adaptive-methods-for-nonconvex-optimization-8186.pdf>
- [47] P. Melchior, R. Joseph, and F. Moolekamp, “Proximal adam: Robust adaptive update scheme for constrained optimization,” 2020. [Online]. Available: <https://arxiv.org/abs/1910.10094>
- [48] A. Paszke, S. Gross, S. Chintala, G. Chanan, E. Yang, Z. DeVito, Z. Lin, A. Desmaison, L. Antiga, and A. Lerer, “Automatic differentiation in pytorch,” 2017.
- [49] U. S. Kamilov, D. Liu, H. Mansour, and P. T. Boufounos, “A recursive born approach to nonlinear inverse scattering,” *IEEE Signal Processing Letters*, vol. 23, no. 8, pp. 1052–1056, 2016.
- [50] G. Osnabrugge, S. Leedumrongwatthanakun, and I. M. Vellekoop, “A convergent born series for solving the inhomogeneous helmholtz equation in arbitrarily large media,” *Journal of Computational Physics*, vol. 322, pp. 113–124, 2016. [Online]. Available: <https://www.sciencedirect.com/science/article/pii/S0021999116302595>
- [51] F. Bureau, J. Robin, A. Le Ber, W. Lambert, M. Fink, and A. Aubry, “Three-dimensional ultrasound matrix imaging,” *Nature Communications*, vol. 14, p. 6793, 2024.
- [52] E. Giraudat, A. Burtin, A. L. Ber, M. Fink, J.-C. Komorowski, and A. Aubry, “Matrix imaging as a tool for high-resolution monitoring of deep volcanic plumbing systems with seismic noise,” *Commun. Earth Environ.*, vol. 5, p. 509, 2024.
- [53] P. Stähli, C. Becchetti, N. Korta Martiartu, A. Berzigotti, M. Frenz, and M. Jaeger, “First-in-human diagnostic study of hepatic steatosis with computed ultrasound tomography in echo mode,” *Communications Medicine*, vol. 3, no. 1, p. 176, Dec. 2023.
- [54] S. Solarino, M. G. Malusà, E. Eva, A. Paul, S. Guillot, S. Pondrelli, S. Salimbeni, and L. Zhao, “Seismic tomography reveals contrasting styles of subduction-channel and mantle-wedge exhumation controlled by upper plate divergent motion,” *Gondwana Research*, vol. 136, pp. 169–182, Dec. 2024.
- [55] L. D’Auria, I. Koulakov, J. Prudencio, I. Cabrera-Pérez, J. M. Ibáñez, J. Barrancos, R. García-Hernández, D. Martínez van Dorth, G. D. Padilla, M. Przeor, V. Ortega, P. Hernández, and N. M. Pérez, “Rapid magma ascent beneath la palma revealed by seismic tomography,” *Scientific Reports*, vol. 12, no. 1, Oct. 2022.
- [56] J. Chaput, M. Campillo, R. C. Aster, P. Roux, P. R. Kyle, H. Knox, and P. Czoski, “Multiple scattering from icequakes at eribus volcano, antarctica: Implications for imaging at glaciated volcanoes,” *Journal of Geophysical Research: Solid Earth*, vol. 120, no. 2, pp. 1129–1141, Feb. 2015.
- [57] A. Goicoechea, C. Brütt, A. Le Ber, F. Bureau, W. Lambert, C. Prada, A. Derode, and A. Aubry, “Reflection measurement of the scattering mean free path at the onset of multiple scattering,” *Physical Review Letters*, vol. 133, no. 17, p. 176301, Oct. 2024.
- [58] J. Virieux and S. Operto, “An overview of full-waveform inversion in exploration geophysics,” *GEOPHYSICS*, vol. 74, no. 6, pp. WCC1–WCC26, Nov. 2009.
- [59] H. Weyl, “Ausbreitung elektromagnetischer wellen über einem ebenen leiter,” *Annalen der Physik*, vol. 365, no. 21, pp. 481–500, 1919.